

# An unusual dimeric structure and assembly for TLR4 regulator RP105–MD-1

Sung-il Yoon<sup>1</sup>, Minsun Hong<sup>1</sup> & Ian A Wilson<sup>1,2</sup>

**RP105–MD-1 modulates the TLR4–MD-2-mediated, innate immune response against bacterial lipopolysaccharide (LPS). The crystal structure of the bovine 1:1 RP105–MD-1 complex bound to a putative endogenous lipid at 2.9 Å resolution shares a similar overall architecture to its homolog TLR4–MD-2 but assembles into an unusual 2:2 homodimer that differs from any other known TLR–ligand assembly. The homodimer is assembled in a head-to-head orientation that juxtaposes the N-terminal leucine-rich repeats (LRRs) of the two RP105 chains, rather than the usual tail-to-tail configuration of C-terminal LRRs in ligand-activated TLR dimers, such as TLR1–TRL2, TLR2–TLR6, TLR3–TLR3 and TLR4–TLR4. Another unusual interaction is mediated by an RP105-specific asparagine-linked glycan, which wedges MD-1 into the co-receptor binding concavity on RP105. This unique mode of assembly represents a new paradigm for TLR complexes and suggests a molecular mechanism for regulating LPS responses.**

Innate immunity plays a critical role in immediately sensing pathogens and subsequently priming adaptive immunity<sup>1,2</sup>. Innate immune responses are initiated by detecting common molecular features of microbial pathogens through pattern recognition receptors including Toll-like receptors (TLRs), Nod-like receptors and RIG-I-like receptors<sup>3,4</sup>. TLRs consist of an extracellular, soluble domain (sTLR), a single-pass transmembrane domain and an intracellular signaling Toll–IL-1R (TIR) domain. The sTLR folds into a horseshoe-like structure with 20–26 leucine-rich repeat (LRR) modules and is responsible for binding a specific ligand<sup>5–9</sup>. However, TLR–ligand binding by itself is not sufficient for signaling. Structural analyses of ligand-bound TLR complexes have suggested that, for TLR activation, ligand binding should induce TLR dimerization in a tail-to-tail mode that juxtaposes their C-terminal regions in the center of the signaling complex<sup>6,8,10,11</sup>. As a result, the intracellular TIR domains are brought into close proximity for downstream signaling.

Among TLR family members, TLR4 is unique in requiring a tightly associated adaptor molecule, MD-2, to recognize bacterial lipopolysaccharide on the cell surface<sup>5,12–14</sup>. sTLR4 forms a heterodimeric complex with MD-2 in its unliganded basal state<sup>5</sup>. MD-2 houses a large hydrophobic cavity, which provides the major LPS binding site<sup>10,15</sup>. LPS binding to MD-2 induces homodimerization of the 1:1 TLR4–MD-2 complex in a tail-to-tail orientation of two TLR4 chains<sup>10</sup>. In contrast, eritoran, an antagonist ligand, binds to the MD-2 cavity but fails to trigger TLR4–MD-2 homodimerization and subsequent signaling<sup>5,16</sup>.

Radioprotective 105, CD180 (RP105) is a TLR-like, cell-surface molecule that is evolutionarily closely related to TLR4 (refs. 17–20). RP105 contains an extracellular LRR domain (sRP105) and a transmembrane domain that share ~30% sequence identity with TLR4. The sRP105 associates with MD-1, an MD-2 homolog (~20% sequence identity), which promotes RP105 cell-surface expression<sup>21–23</sup>. Unlike

TLR4, RP105 contains only about ten intracellular residues and lacks the canonical TIR signaling domain, suggesting that RP105–MD-1 by itself cannot transmit an extracellular signal into cells.

RP105–MD-1 exerts dichotomous regulatory activities on TLR4-mediated LPS responses depending on cell type. RP105-deficient B cells show impairment in LPS responses such as cell proliferation and IgM- and IgG3 antibody production<sup>24,25</sup>, suggesting that RP105–MD-1 is a B-cell stimulator, although its stimulatory mechanism in B cells is largely unknown. In contrast, in antigen-presenting cells, including dendritic cells and macrophages, RP105–MD-1 downregulates LPS responses through a direct interaction with TLR4–MD-2 (refs. 20,26,27). In addition, RP105–MD-1 can enhance TLR2 activity against *Mycobacterium tuberculosis* lipoproteins through TLR2 interaction in macrophages<sup>28</sup>. Thus, RP105–MD-1 appears to fine-tune the ligand-induced activities of TLRs as a regulatory complex rather than by directly and solely initiating a signal.

Given that RP105–MD-1 is homologous to TLR4–MD-2, it has been generally assumed that RP105–MD-1 would adopt a similar complex structure to TLR4–MD-2. However, as the RP105 structure or the structural basis for RP105–MD-1 association was not known, the molecular mechanism for RP105–MD-1 regulation of the TLR4–MD-2 activity could not be addressed. Thus, we determined the crystal structure of the bovine sRP105–MD-1 complex to 2.91 Å resolution. Unexpectedly, the structure reveals that sRP105–MD-1 forms an unusual tetrameric complex of two sRP105 and two MD-1 molecules. Despite an identical molecular stoichiometry (2:2) to that of the LPS-activated sTLR4–MD-2 complex, sRP105–MD-1 uses distinctively different binding interfaces for complex formation. As a result, sRP105 and MD-1 are organized in a unique mode that positions the N-terminal LRR modules of two sRP105 chains in the center of the complex, together with two MD-1 molecules. This head-to-head

<sup>1</sup>Department of Molecular Biology, The Scripps Research Institute, La Jolla, California, USA. <sup>2</sup>The Skaggs Institute for Chemical Biology, The Scripps Research Institute, La Jolla, California, USA. Correspondence should be addressed to I.A.W. (wilson@scripps.edu).

Received 24 December 2010; accepted 14 June 2011; published online 21 August 2011; doi:10.1038/nsmb.2106

arrangement of RP105 contrasts with the tail-to-tail mode that is highly conserved in ligand-activated TLR homo- and heterodimers<sup>6,8,10,11</sup>. The unique organization of this sRP105–MD-1 complex allows us to propose a mechanism for how the TLR4 response to LPS is regulated. Furthermore, the sRP105–MD-1 structure reveals that an RP105-specific, asparagine-linked glycan provides an additional extensive site of interaction that is not present in the TLR4–MD-2 complex and represents an uncommon use of glycans in protein–protein interfaces.

## RESULTS

### Overall architecture of the 2:2 sRP105–MD-1 complex

sRP105 and MD-1 were coexpressed in insect cells by a baculovirus expression system and purified as a stable complex. Gel-filtration analysis demonstrated that purified human, mouse and bovine sRP105–MD-1 complexes elute at a size larger than the unliganded 1:1 sTLR4–MD-2 complex but similar to the LPS-activated 2:2 sTLR4–MD-2 complex (Supplementary Fig. 1a), suggesting a 2:2 stoichiometry.

The crystal structure of the bovine sRP105–MD-1 (residues 24–626 and 22–159, respectively) complex was determined at 2.91 Å resolution (Fig. 1 and Supplementary Fig. 1b,c). The structure unambiguously reveals that the complex is assembled from two sRP105 and two MD-1 molecules in an inverted ‘ω’ shape (Fig. 1). sRP105 and MD-1 adopt horseshoe and β-cup-like shapes, similarly to sTLR4 and MD-2, respectively (Fig. 2)<sup>5,15</sup>. The sRP105–MD-1 complex consists of two copies of the 1:1 building block (sRP105<sub>a</sub>–MD-1<sub>a</sub> or sRP105<sub>b</sub>–MD-1<sub>b</sub> in Fig. 1), each of which resembles the unliganded 1:1 sTLR4–MD-2 complex in overall architecture<sup>5</sup>, but the assembly of the 2:2 tetramer distinguishes it from other agonist-activated TLR complexes (see below). In the 2:2 sRP105–MD-1 complex, two sRP105 molecules are arranged in a head-to-head orientation that places their N-terminal regions in the center of the complex, while simultaneously interacting with two MD-1 molecules (Fig. 1). Such a unique organization of sRP105 and MD-1 in the complex was further confirmed by a 3.1-Å resolution structure of a complex between MD-1 and an LRR hybrid of sRP105 (residues 24–521) fused with variable lymphocyte receptor (VLR) B.61 (residues 125–200) (Table 1).

### Structure of sRP105

sRP105 folds into a typical horseshoe-like structure with the central LRR core (LRR modules 1–22) shielded by N-terminal (LRRNT) and C-terminal (LRRCT) LRR caps (Fig. 2a and Supplementary Fig. 2a)<sup>5,7,9</sup>. sRP105 is divided into three subdomains, namely N-terminal (LRRNT and LRR1–LRR6), central (LRR7–LRR12) and C-terminal (LRR13–LRR22 and LRRCT) (Fig. 2a), as described for sTLR4, although sRP105 shows less obvious structural transitions at interdomain boundaries compared to sTLR4 (ref. 5). On the concave face of the horseshoe-like sRP105 structure, a continuous β-sheet is formed by 22 parallel β-strands of the LRR core as well as two antiparallel β-strands of the LRRNT β-hairpin. By comparison, the convex surface is irregularly

decorated with various secondary structures, including α-helices,  $3_{10}$ -helices and short β-strands. The sRP105 contains six disulfide bonds, five of which are conserved with sTLR4. The remaining disulfide bond between Cys337 and Cys365 is specific to sRP105, and links LRR12 and LRR13 loops that are three residues longer than those of sTLR4, thereby potentially stabilizing otherwise mobile loops.

sRP105 adopts a more circular and flat profile than sTLR4 (Supplementary Fig. 2b). The curvature in sRP105 is more pronounced for its C-terminal LRR modules, presumably because of the presence of an α-helix in the LRR21 convex face (Fig. 2a and Supplementary Fig. 2b, left) that is wider than the extended chain or  $3_{10}$ -helix segments located in the corresponding region of TLR4 (refs. 29–31). As a result, sRP105 shows a more closed circular shape (LRR1–LRR22 distances: sRP105, 31 Å; human sTLR4, 43 Å; mouse sTLR4, 38 Å) (Supplementary Fig. 2b, left). From the side profile, sRP105 is more or less flat, whereas sTLR4 is severely twisted in its N-terminal domain, which leads to 19° and 8° deviations of sRP105 from mouse and human sTLR4, respectively, when their N-terminal domains are superimposed (Supplementary Fig. 2b, right).

### Structure of MD-1

As observed in previous MD-1 structures (MD-1<sub>free</sub>) in the absence of RP105 (chicken MD-1<sub>free</sub>, cMD-1<sub>free</sub> and mouse MD-1<sub>free</sub>, mMD-1<sub>free</sub>)<sup>32,33</sup>, sRP105-bound MD-1 (MD-1<sub>sRP105</sub>) adopts a β-cup-like structure that consists of two antiparallel β-sheets (β-strands C, D, G and β-strands A, B, I, H, E, F) and contains three disulfide bonds (Cys30–Cys55, Cys42–Cys151 and Cys99–Cys109) that stabilize the β-cup-like structure (Fig. 2b and Supplementary Fig. 2c)<sup>32,33</sup>. The MD-1 loops are designated by their connecting β-strands (for example, the AB loop connects β-strands A and B). MD-1<sub>sRP105</sub> also houses a large hydrophobic cavity between its two β-sheets that is mainly lined with hydrophobic residues, although four polar residues (Lys105, Asn124, Asn125 and Glu129) are positioned at the cavity entrance (Supplementary Fig. 2d). The MD-1<sub>sRP105</sub> cavity contains additional

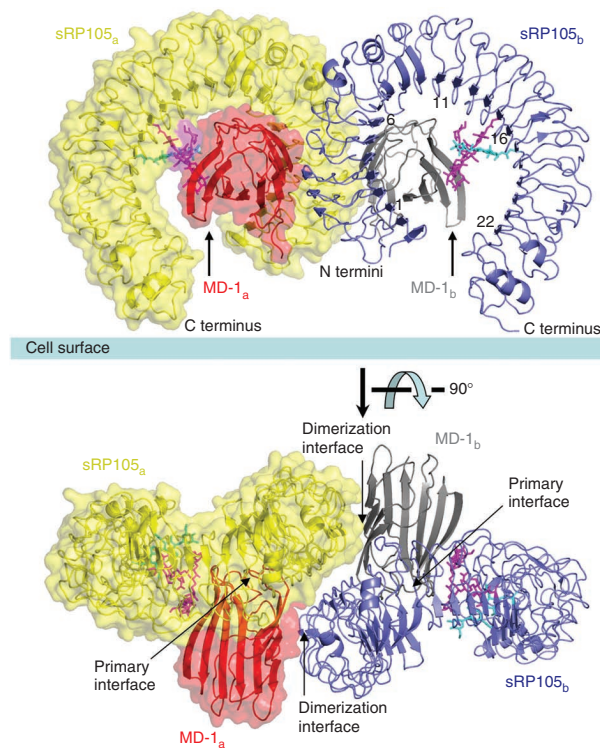
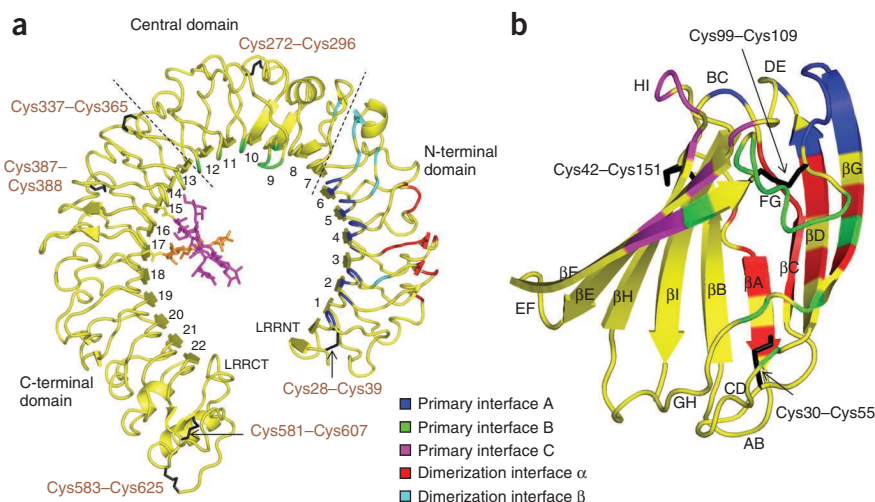


**Figure 1** Overall architecture of the 2:2 sRP105–MD-1 complex. The 1:1 sRP105–MD-1 building block that corresponds to unliganded 1:1 sTLR4–MD-2 complex is designated by sRP105<sub>a</sub>–MD-1<sub>a</sub> (yellow and red; translucent molecular surface with underlying ribbon representation) or sRP105<sub>b</sub>–MD-1<sub>b</sub> (blue and gray; ribbon only). The 1:1 complex formation is driven by the primary binding interface between RP105 and MD-1. Two copies of the 1:1 complex associate in a symmetrical manner in a head-to-head mode through a unique dimerization interface. RP105 Asn402- and Asn451-linked glycans that are well ordered in the sRP105<sub>a</sub>–MD-1<sub>a</sub> or sRP105<sub>b</sub>–MD-1<sub>b</sub> interface region are shown in magenta and cyan stick models, respectively. The two views are shown parallel to the cell surface (above) and from the top looking down onto the cell surface (below).

**Figure 2** sRP105 and MD-1 structures as observed in the 2:2 complex. (a,b) The sRP105 (a) and MD-1 (b) structures are represented by yellow ribbon diagrams, and the components of the structure that form each binding interface are colored as indicated in the figure. RP105 residues are labeled in brown. The asparagine-linked glycan at sRP105 Asn402, which is involved in primary interface C, is shown in magenta sticks and the nearby glycan at Asn451 is colored orange. Disulfide bonds are shown in black sticks. sRP105 is divided into three subdomains as indicated by dashed lines that correspond to those designated in previous work in TLR4 as the N-terminal, central and C-terminal domains<sup>10</sup>.



electron density that was modeled as two connected acyl chains of an endogenous pseudoligand that was presumably acquired during protein expression (**Supplementary Fig. 2d**).

Likewise, MD-1<sub>free</sub> also contains an endogenous ligand, potentially a diacylated phospholipid molecule<sup>32,33</sup>. These observations indicate that MD-1 has affinity for lipid ligands irrespective of whether RP105 is bound. Despite the expected overall structural conservation between MD-1<sub>free</sub> and MD-1<sub>sRP105</sub>, substantial differences are found in the conformation and flexibility of the FG and GH loops at the cavity entrance (**Supplementary Fig. 2e**), suggesting some dynamic behavior dependent on the state of ligation, whether with RP105 or lipid<sup>32,33</sup>.

### Primary binding interfaces A and B

sRP105–MD-1 assembly can be described as containing primary binding and dimerization interfaces (**Fig. 1**). sRP105 and MD-1 form the 1:1 complex through the primary interface and homodimerize to a 2:2 complex using the dimerization interface. For the primary interaction, the concave surface of sRP105 wraps around one end of MD-1, mainly at  $\beta$ F, loop FG,  $\beta$ G and loop HI (**Figs. 2** and **3a**). The primary interaction buries  $\sim 1,290 \text{ \AA}^2$  of accessible surface area on each component and is segregated into three discontinuous regions corresponding to primary binding interfaces A, B and C (**Fig. 3** and **Supplementary Fig. 3a**). Primary interfaces A and B involve protein-only contacts of the sRP105 N-terminal and central domains, respectively, with MD-1 (**Fig. 2a**), and these contact regions are mostly conserved in TLR4–MD-2. However, primary interface C is created by an asparagine-linked glycan on the concave face of the sRP105 C-terminal domain and is unique to the RP105–MD-1 interaction (**Fig. 2a**).

In primary binding interface A, 15 residues on the sRP105 N-terminal domain bury  $\sim 500 \text{ \AA}^2$  of accessible surface area through contact with ten MD-1 residues (**Fig. 3b** and **Supplementary Fig. 3a**). A set of highly conserved MD-1 residues from loop FG (Arg111, Arg112, Lys113, Gly114, Glu115),  $\beta$ G (Gln116) and loop DE (Arg72) make extensive contacts with sRP105 residues scattered throughout the concave side of LRRNT and LRR1–LRR6. The interaction is mainly polar, including six hydrogen bonds and one salt bridge, but it also includes van der Waals contacts between three spatially adjacent sRP105 threonine residues (Thr85, Thr109, Thr133) and three successive MD-1 residues (Lys113, Gly114, Glu115).

Primary binding interface B is formed by interaction between ten residues on sRP105 LRR9–LRR13 and 11 MD-1 residues mainly from  $\beta$ F, loop FG and  $\beta$ G, burying  $\sim 410 \text{ \AA}^2$  of accessible surface area on each side (**Fig. 3c** and **Supplementary Fig. 3a**). The major interaction occurs between a protruding loop of LRR9 and eight MD-1 residues, where three LRR9 residues (Phe255, Glu256 and Asp257) contribute to  $\sim 60\%$  of the

buried surface area and form three hydrogen bonds to MD-1 Lys105 (carbonyl) and Ser107 (amide and hydroxyl).

The primary binding interfaces A and B of sRP105–MD-1 involve similar protein surfaces or residues as in sTLR4–MD-2 (**Supplementary Fig. 3b**)<sup>5,10</sup>, but several structural features are distinguishable. First, the charge complementarity observed in the primary sTLR4–MD-2 interaction is less pronounced in sRP105–MD-1 (**Supplementary Fig. 3c**). In primary binding interface A of mouse sTLR4–MD-2, MD-2 Arg68 makes a salt bridge with sTLR4 Asp41, and MD-2 Lys109 makes ionic

**Table 1** Data collection and refinement statistics

	sRP105-VLR–MD-1	sRP105–MD-1
<b>Data collection</b>		
Space group	$P2_12_12_1$	$P1$
Cell dimensions		
<i>a</i> , <i>b</i> , <i>c</i> (Å)	89.58, 137.52, 141.67	101.51, 141.58, 141.95
$\alpha$ , $\beta$ , $\gamma$ (°)	90.00, 90.00, 90.00	94.00, 91.66, 91.37
Resolution (Å)	20.00–3.10 (3.21–3.10)	20.00–2.91 (3.00–2.91)
$R_{\text{merge}}$	9.0 (80.3)	6.3 (45.7)
$I / \sigma I$	34.3 (2.8)	18.2 (1.8)
Completeness (%)	98.9 (93.1)	93.5 (73.0)
Redundancy	8.1 (7.1)	2.1 (1.9)
<b>Refinement</b>		
Resolution (Å)		20.00–2.91
No. reflections		152,067
$R_{\text{work}} / R_{\text{free}}$		23.8 / 27.6
No. atoms		
Protein		42,570
Carbohydrate		1,064
Pseudoligand		124
Water		37
<i>B</i> -factors		
Protein		76.4
Carbohydrate		49.4
Pseudoligand		81.9
Water		42.9
r.m.s. deviations		
Bond lengths (Å)		0.013
Bond angles (°)		1.43

Values in parentheses are for highest-resolution shell. Data for the sRP105–MD-1 structure were collected from a single crystal.

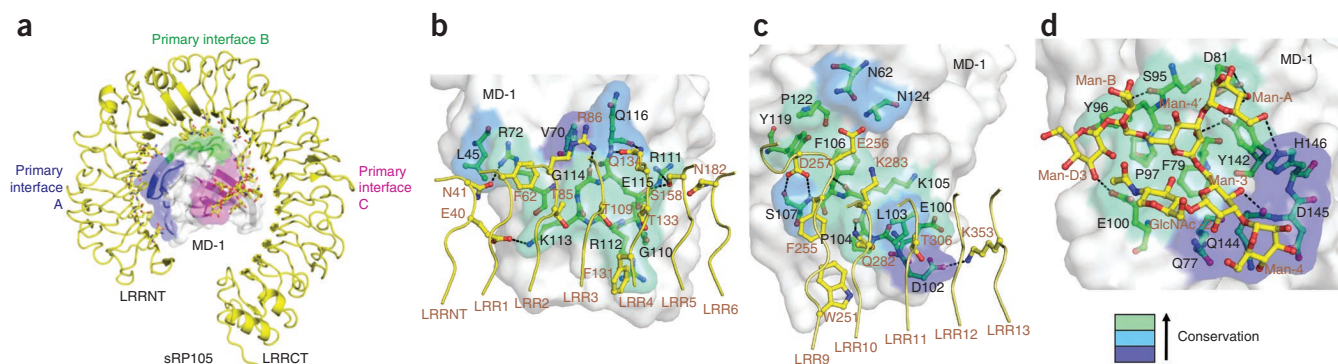


**Figure 3** The sRP105–MD-1 primary interaction. (a) Overall view of the 1:1 sRP105–MD-1 complex. The 1:1 complex is represented by a ribbon diagram (sRP105, yellow; MD-1, gray) and primary interfaces A, B and C are colored in blue, green and magenta, respectively, on the MD-1 surface. sRP105 primary interface residues are shown in stick models (carbon, yellow; oxygen, red; nitrogen, blue). (b–d) Close-up view of primary interfaces A (b), B (c) and C (d). Interfaces A and B correspond to A patch and B patch, respectively, as designated in previous work in TLR4–MD-2 (ref. 5). MD-1 and sRP105 residues in the primary interface are shown in green and yellow ball-and-stick models, respectively, with oxygens in red and nitrogens in blue. The MD-1 interface is color-coded on a surface representation according to sequence conservation among ten MD-1 orthologs from light green (most conserved) to dark blue (less conserved). Broken dotted lines represent hydrogen bonds or salt bridges. RP105 residues are labeled in brown.

interactions with sTLR4 Asp59 and Asp83. In the sTLR4–MD-2 primary binding interface B, three acidic MD-2 residues (Asp99, Asp100, Asp101) are surrounded by four basic sTLR4 residues (Arg233, Lys263, Arg288, Arg337), with an additional salt bridge between MD-2 Arg106 and sTLR4 Asp208. These extensive interactions suggest that charge complementarity is a major contributor to the sTLR4–MD-2 interaction. However, in the sRP105–MD-1 interface, only two salt bridges (Glu40–Lys113 and Lys353–Asp102) are found. Moreover, Asp102 of bovine MD-1 corresponds to Ala105 in human MD-1 that cannot form the salt bridge (Supplementary Fig. 2c). Second, the total buried surface area of primary binding interfaces A and B in sRP105–MD-1 (1,810 Å<sup>2</sup>) is smaller than in mouse (2,280 Å<sup>2</sup>) or human (2,030 Å<sup>2</sup>) sTLR4–MD-2 owing to a lack of interaction between sRP105 LRR7–LRR8 and MD-1 (Supplementary Fig. 3a, bottom). Third, sRP105–MD-1's hydrophilic interactions (12 hydrogen bonds) are fewer than in mouse (18) and human (24) sTLR4–MD-2 (Supplementary Fig. 3b). Thus, these observations suggest that the contribution of protein–protein interactions from binding interfaces A and B to the overall binding interface in sRP105–MD-1 is less than in TLR4–MD-2.

To define the structural basis for binding specificity of RP105 for MD-1 and TLR4 for MD-2, primary binding interfaces of both complexes were carefully analyzed. In the sTLR4–MD-2 structure, the negatively charged Asp101 in MD-2 forms an ionic interaction with the positively charged Lys263 in mouse sTLR4 or Arg264 in human sTLR4 (Supplementary Figs. 2a,c and 3c, right). In sRP105–MD-1, the electrostatic charge pattern is the opposite, with MD-1, contributing a positively charged Lys105 and sRP105 providing the acidic residue Glu256 (Supplementary Fig. 2a,c), suggesting that a charge–charge repulsion may disfavor complex formation between RP105 and MD-2 and between TLR4 and MD-1. Furthermore, steric complementarity also rules out possibilities for such cross-reactivity, as severe steric clashes are observed between sRP105 LRR9–LRR10 and the rigid MD-2 loop FG at and around a 3<sub>10</sub> helix when MD-2 is superimposed onto the RP105–MD-1 structure.

### The unique primary binding interface C

In the 1:1 sRP105–MD-1 structure, a triantennary glycan, which is N-linked to RP105 Asn402 at LRR15 on the concave surface (Supplementary Fig. 2a), makes extensive interactions with MD-1, creating primary binding interface C (Figs. 1, 3d and 4a).

When glycoproteins, such as sRP105–MD-1, are expressed in insect cells, asparagine-linked glycans are processed from Glc<sub>3</sub>Man<sub>9</sub>GlcNAc<sub>2</sub> tetradecasaccharide, through Man<sub>9</sub>GlcNAc<sub>2</sub> and Man<sub>5</sub>GlcNAc<sub>2</sub>, to fucosylated or nonfucosylated Man<sub>3</sub>GlcNAc<sub>2</sub> pentasaccharides<sup>34,35</sup> (Fig. 4b). However, the RP105 Asn402-linked glycan shows unequivocal electron density for a triantennary high-mannose glycan (D1, D2, D3 arms) that is occasionally observed in insect cell glycoproteins and has been modeled as Man<sub>6</sub>GlcNAc<sub>2</sub> (Fig. 4)<sup>35</sup>. Additional weak residual electron density beyond terminal Man-A and Man-4 sugars suggests that the actual glycan attached to Asn402 is Man<sub>8–9</sub>GlcNAc<sub>2</sub> (Fig. 4a).

Although asparagine-linked glycans are usually highly flexible, this sRP105 glycan is well ordered (average B-value ~49 Å<sup>2</sup>) through extensive polar interactions with surrounding sRP105–MD-1 protein residues (~53 Å<sup>2</sup>) and another neighboring glycan (~51 Å<sup>2</sup>) (Figs. 3d and 4a). The two core GlcNAc moieties hydrogen-bond with the RP105 glycan at Asn451, as well as with Ser378, His379, Tyr400 and Asp426 side chains. The terminal Man (D3) on the D3 arm hydrogen-bonds to the His379 main chain carbonyl (Fig. 4a). These interactions help orient the glycan toward MD-1, which further stabilizes the glycan conformation.

In primary binding interface C, seven sugars (GlcNAc-2 and Man-3, Man-4, Man-4', Man-A, Man-B and Man-D3) interact with 11 residues from MD-1 β-strands E, F, H and loops DE, HI. The interaction involves eight hydrogen bonds and buries ~370 Å<sup>2</sup> of MD-1 surface area, which is comparable to that in primary interface A or B (Fig. 3d). The glycan-interacting residues on MD-1 are largely conserved (Fig. 3d and Supplementary Fig. 2c). Furthermore, the Asn402 glycosylation site and stabilizing residues, including Ser378, His379, Asp426 and Asn451, are completely conserved among RP105 orthologs (Supplementary Fig. 2a).

The glycan-mediated protein–protein interaction is specific to RP105–MD-1, as no glycans are found in the sTLR4–MD-2 interface, and the residue corresponding to sRP105 Asn402 is aspartate in all known mammalian TLR4 orthologs (Supplementary Fig. 2a). The only other example of glycan involvement in TLR interactions is found in TLR3, where the glycan at Asn413, modeled as Man<sub>3</sub>GlcNAc<sub>2</sub>, contacts the ribose backbone of its dsRNA ligand, but only one terminal Man is involved that buries ~70 Å<sup>2</sup> of dsRNA surface area (Supplementary Fig. 4a).

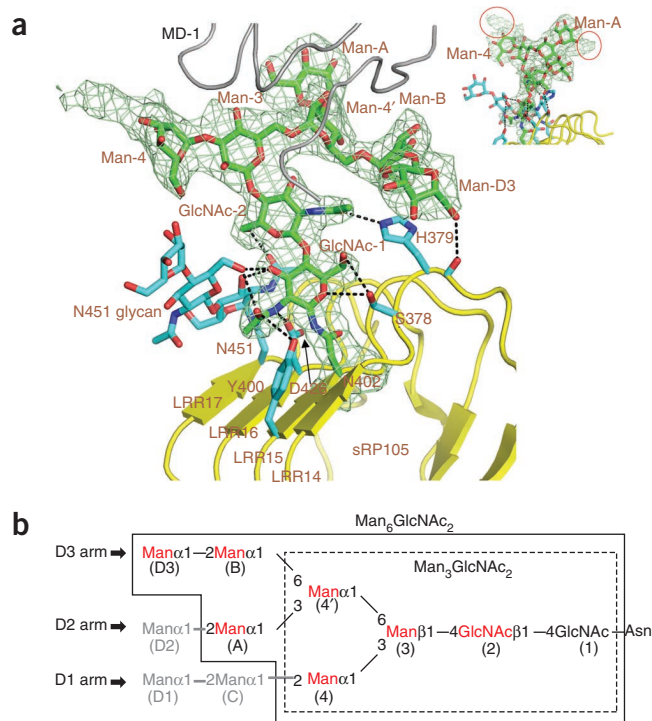


**Figure 4** sRP105-specific glycan at Asn402. (a) Asn402-linked glycan (green sticks) is stabilized by interactions with neighboring sRP105 protein residues, as well as with Asn451-linked glycan (cyan sticks). Hydrogen bonds are represented by dashed lines. Electron density for the Asn402-linked glycan is shown in a pale green mesh at a  $1.0\text{-}\sigma$  level in a  $2F_o - F_c$  map. The sRP105 and MD-1 C $\alpha$  traces are colored in yellow and gray, respectively. Residual electron density observed beyond Man-A and Man-4 sugars of glycan at Asn402 are circled in red in the inset (top right) and suggest that the glycan is Man<sub>8-9</sub>GlcNAc<sub>2</sub>. RP105 residues are labeled in brown. (b) Schematic diagram of an asparagine-linked high mannose glycan, Man<sub>9</sub>GlcNAc<sub>2</sub>. The most frequently found asparagine-linked glycan in insect cells, Man<sub>3</sub>GlcNAc<sub>2</sub>, is boxed in dashed lines. Asn402-linked glycan (Man<sub>6</sub>GlcNAc<sub>2</sub>) that could be modeled well in the sRP105 structure is enclosed by solid lines. Glycan residues that make contacts with MD-1 are labeled in red. The standard nomenclature of each sugar moiety is shown in parentheses.

**Supplementary Fig. 5a).** Three hydrophobic residues (Trp91, Ile114, Phe115) from RP105 LRR2 and LRR3 protrude into a shallow groove on MD-1  $\beta$ C and  $\beta$ D, and they interact mainly with Gly49 and Gly68 (Fig. 5b). This central interaction is buttressed by peripheral polar interactions including four hydrogen bonds and one salt bridge, as well as an aromatic, perpendicular stacking interaction between Tyr118 and Phe142.

Interface  $\beta$  involves symmetric interactions of sRP105<sub>a</sub> and sRP105<sub>b</sub> from the ascending side of LRR2 and LRR5–LRR7 (Figs. 2 and 5c). Each sRP105 chain buries a relatively small surface area of only  $\sim 180\text{ \AA}^2$  in interface  $\beta$  (Supplementary Fig. 5a, top), using only van der Waals interactions (Fig. 5c). In addition, interface  $\beta$  shows poor shape complementarity ( $S_c$  value of 0.35) compared to other interfaces (primary interface A, 0.67; primary interface B, 0.68; dimerization interface  $\alpha$ , 0.69)<sup>36</sup>. Thus, interface  $\beta$  makes relatively minor contributions compared to interface  $\alpha$ .

#### Comparison with agonist-activated TLR dimers

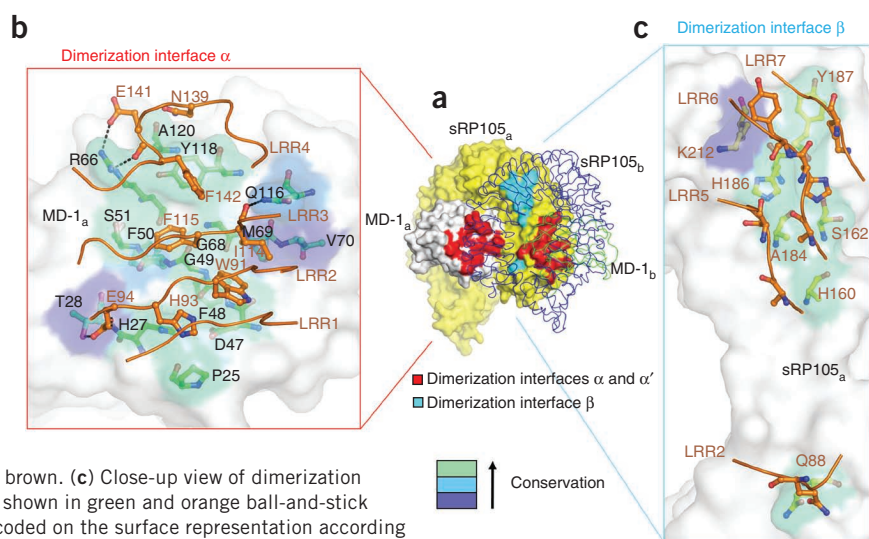
Despite the same 2:2 molecular stoichiometry of sRP105–MD-1 and LPS-bound sTLR4–MD-2, they have completely different dimerization interfaces and arrangements of their TLR or TLR-like structures (Fig. 6a–d). In sRP105–MD-1, each MD-1 molecule uses contiguous primary and dimerization interfaces to simultaneously engage the concave face of N-terminal LRR1–LRR4 modules from one sRP105 chain and the convex face of the same LRR modules from the second sRP105 chain, respectively (Fig. 6c). Consequently, the N-terminal

#### The dimerization binding interface

The dimerization interface is involved in assembly of two copies of the 1:1 sRP105–MD-1 complex (sRP105<sub>a</sub>–MD-1<sub>a</sub> and sRP105<sub>b</sub>–MD-1<sub>b</sub>) into the 2:2 complex through noncrystallographic, two-fold symmetry between the two 1:1 complexes (Fig. 1). This homodimerization interface contains three separate interaction surfaces: sRP105<sub>a</sub>–MD-1<sub>b</sub> interface  $\alpha$ , its two-fold-related sRP105<sub>b</sub>–MD-1<sub>a</sub> interface  $\alpha'$  and sRP105<sub>a</sub>–sRP105<sub>b</sub> interface  $\beta$  (Fig. 5a). This dimerization interface is composed from 19 highly conserved residues from sRP105 and 15 from MD-1, with  $\sim 1,230\text{ \AA}^2$  of total buried surface area (Supplementary Fig. 5a,b).

Dimerization interface  $\alpha$  is located on the convex surface of sRP105 LRR1–LRR4 and on  $\beta$ A,  $\beta$ C,  $\beta$ D,  $\beta$ G, loop BC and the N-terminal region of MD-1, burying  $\sim 560\text{ \AA}^2$  of sRP105 surface area (Figs. 2 and 5b and

**Figure 5** The unique sRP105–MD-1 homodimerization interaction for assembly of the 2:2 complex. (a) Overall view of the 2:2 sRP105–MD-1 complex. 1:1 sRP105<sub>a</sub>–MD-1<sub>a</sub> and sRP105<sub>b</sub>–MD-1<sub>b</sub> complexes are shown in a surface representation (yellow sRP105<sub>a</sub>, gray MD-1<sub>a</sub>) and in thin coils (blue sRP105<sub>b</sub>, green MD-1<sub>b</sub>), respectively. The dimerization interface is colored in red (interfaces  $\alpha$  and  $\alpha'$ ) and cyan (interface  $\beta$ ) on the surface representation of the sRP105<sub>a</sub>–MD-1<sub>a</sub>. (b) Close-up view of dimerization interface  $\alpha$ . MD-1<sub>a</sub> and sRP105<sub>b</sub> residues are shown with green and orange carbons (red oxygens, blue nitrogens) in ball-and-stick models, respectively. The MD-1<sub>a</sub> interface is color-coded on the surface representation by sequence conservation as in Figure 3. Broken dotted lines represent hydrogen bonds or salt bridges. RP105 residues are labeled in brown. (c) Close-up view of dimerization interface  $\beta$ . The sRP105<sub>a</sub> and sRP105<sub>b</sub> residues are shown in green and orange ball-and-stick models, respectively. The RP105<sub>a</sub> interface is color-coded on the surface representation according to sequence conservation in four RP105 orthologs.



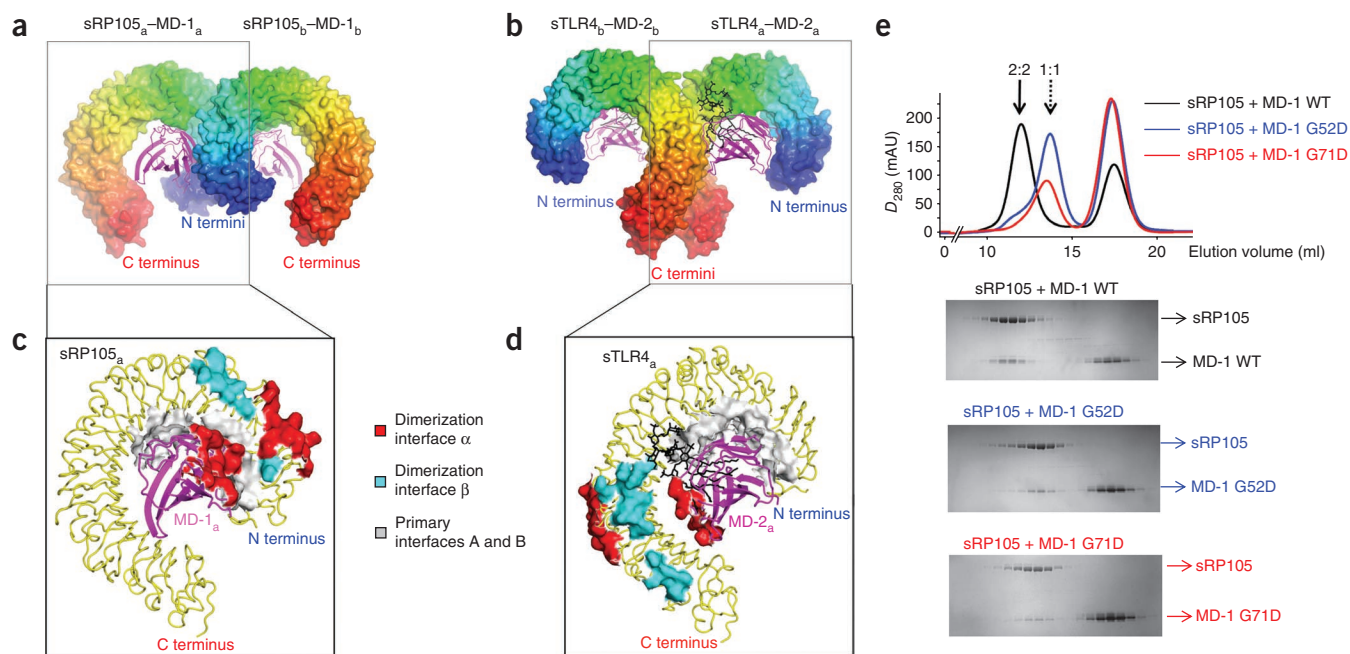


**Figure 6** Different organization of the 2:2 sRP105–MD-1 and LPS-bound 2:2 sTLR4–MD-2 homodimeric assemblies. **(a,b)** The head-to-head homodimer of 2:2 sRP105–MD-1 **(a)** and the tail-to-tail homodimer of LPS-bound 2:2 TLR4–MD-2 (PDB 3FXI)<sup>10</sup> **(b)**. The surface representations of sRP105 and sTLR4 are rainbow-colored from N terminus (blue) to C terminus (red). MD-1 and MD-2 are shown in magenta ribbons. LPS bound to sTLR4–MD-2 is represented by black sticks. **(c,d)** Close-up views of 1:1 sRP105<sub>a</sub>–MD-1<sub>a</sub> **(c)** and 1:1 sTLR4<sub>a</sub>–MD-2<sub>a</sub> **(d)**. The distinct dimerization interfaces of 2:2 sRP105–MD-1 and TLR4–MD-2 are shown as red and cyan surface representations over the ribbon diagram of their respective 1:1 complexes. For comparison, the similar primary interfaces A and B are shown in gray surface representations. **(e)** The unique head-to-head arrangement of sRP105–MD-1 is verified by mouse MD-1 mutants G52D and G71D, which do not permit homodimerization of the sRP105–MD-1 complex. sRP105 coexpressed with an excess of MD-1 WT or mutants was analyzed by gel-filtration chromatography (top), and its fractions were resolved by SDS-PAGE (bottom). mAU, milliabsorbance units.

LRR modules of the two sRP105 chains are positioned, along with MD-1, in the center of the complex in a head-to-head orientation (Fig. 6a). In the LPS-bound 2:2 sTLR4–MD-2 complex, MD-2 uses spatially separated surfaces for the primary and dimerization interactions (Fig. 6d). MD-2 forms primary interactions using the same face with the N-terminal LRR modules of sTLR4 as MD-1 does with RP105, but uses its opposite face to make homodimerizing contacts with the C-terminal modules (LRR15–LRR17) from the second TLR4 chain, rather than with the N-terminal LRRs (Fig. 6d). As a result, the two C-terminal domains of sTLR4 interact in a tail-to-tail arrangement that brings their intracellular C-terminal signaling domains together (Fig. 6b)<sup>10</sup>. Such a tail-to-tail TLR arrangement is recapitulated in other agonist-activated sTLR dimers, including dsRNA-bound sTLR3 homodimer and lipopeptide-bound sTLR2–sTLR1 or sTLR2–sTLR6 heterodimers (Supplementary Fig. 6)<sup>6,8,11</sup>. Taken together, these results show that sRP105–MD-1, in the absence of added LPS, forms preassembled homodimers in a head-to-head organization through contiguous primary and dimerization interfaces, whereas sTLR4–MD-2, in the presence of LPS, homodimerizes in a tail-to-tail mode using spatially separated interfaces.

This unique quaternary binding interaction of sRP105–MD-1 has not been found to date in other TLRs. The uniqueness of RP105–MD-1 homodimerization interaction is substantiated by higher sequence conservation in RP105–MD-1 residues in the homodimerization interface than in their equivalent TLR4–MD-2 residues (Supplementary Fig. 5b,c) and lower conservation in RP105–MD-1 residues that correspond to the TLR4–MD-2 homodimerization interface (Supplementary Fig. 5d,e). To further verify the RP105–MD-1 homodimerization interaction, mouse MD-1 mutants G52D and G71D were designed to disrupt this interaction. Mouse MD-1 Gly52 and Gly71 correspond to

bovine MD-1 Gly49 and Gly68, respectively, which have a critical role in accommodating hydrophobic residues from sRP105 in the center of dimerization interface  $\alpha$ . Consistent with our structural observation, both MD-1 G52D and MD-1 G71D were almost completely devoid of homodimer formation, but they retained the sRP105–MD-1 primary interaction, as suggested by formation of a stable 1:1 complex between the mutant MD-1 and sRP105 (Fig. 6e). This mutational study, combined with the crystal structure, demonstrates that the sRP105–MD-1 dimerization interaction is not species-specific and is conserved, at least in mouse and bovine sRP105–MD-1. Furthermore, these results are consistent with the two sRP105 molecules being arranged in the head-to-head orientation through the unique dimerization interaction with MD-1.

## DISCUSSION

Here, we provide compelling crystallographic, biophysical and mutational evidence that sRP105 forms a unique tetrameric complex with MD-1 through primary and homodimerization interfaces. Although the primary interaction engages RP105 and MD-1 in a similar orientation as TLR4–MD-2, several structural differences are observed. The sRP105–MD-1 primary interaction does not show as strong a charge complementarity as that of sTLR4–MD-2 and thus may have lower affinity and specificity. This protein-protein interface (interface A and interface B) is supplemented by a unique RP105–MD-1-specific glycan-protein interface (interface C) between RP105 Asn402-linked glycan and MD-1. The relatively large buried surface area and the sequence conservation within this glycan-protein interface would suggest its importance in sRP105–MD-1 association, but we have not been able to quantitate this interaction, as the sRP105 N402Q mutant does not express well and is probably misfolded.

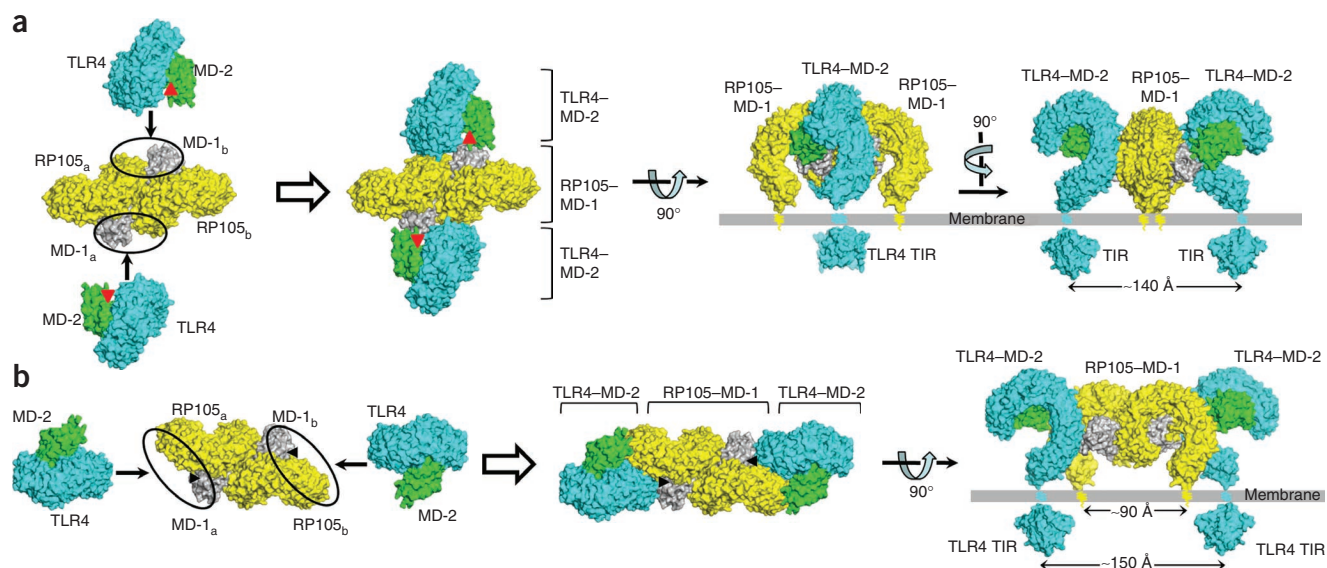


**Figure 7** Two possible models for the interaction between RP105–MD-1 and TLR4–MD-2. **(a,b)** Binding models 1 **(a)** and 2 **(b)**. Potential TLR4–MD-2 binding sites on RP105–MD-1 are highlighted by black circles in left panels, and their resulting complexes are shown in right panels. The sRP105–MD-1 (yellow and gray) and sTLR4–MD-2 (cyan and green) structures are shown by surface representations. MD-2 **(a)** and MD-1 **(b)** cavities that accommodate LPS molecules are represented by red and black triangles, respectively. Currently, we favor model 2.

Nevertheless, coexpression of RP105 N402Q with MD-1 does lead to formation of relatively stable 2:2 complexes.

RP105 Asn402 glycan adopts a partially processed, high-mannose type sugar, rather than the  $\text{Man}_3\text{GlcNAc}_2$  that is commonly observed in insect cells<sup>34,35</sup>. The incomplete processing may be attributable to Asn402's highly restricted location in the sRP105–MD-1 complex. The Asn402 glycan is wedged between MD-1 and the concave face of sRP105 (**Supplementary Fig. 4b**) and would be sterically inaccessible to glycan-processing enzymes in the endoplasmic reticulum or Golgi apparatus, resulting in retention of a high-mannose sugar. Accordingly, mammalian-cell Asn402 glycan expressed *in vivo* would also favor high-mannose glycans, rather than highly processed complex-type glycans. Notwithstanding, when we modeled a complex glycan *in silico*, in place of the high-mannose glycan, most of the crucial interactions with MD-1 were conserved without noticeable steric clashes.

Although RP105–MD-1 forms a homodimer, as in ligand-activated TLRs, its configuration is completely different. All of the structures of ligand-bound TLR dimers determined to date show a tail-to-tail organization, which places the C termini of two sTLRs in close proximity ( $\sim 25$  Å) to activate signaling<sup>6,8,10,11</sup>. In contrast, 2:2 sRP105–MD-1 engages its two sRP105 molecules in a head-to-head orientation, resulting in a large distance ( $\sim 90$  Å) between their C termini. The distant positioning of sRP105 C termini in the complex, as well as a lack of a signaling TIR domain in RP105, suggests that RP105 cannot directly transduce any signal in cells.

RP105–MD-1 exerts its regulatory activity on LPS and lipoprotein responses by directly interacting with TLR4–MD-2 and TLR2, respectively<sup>20,26,28</sup>. In particular, inhibition of LPS responses occurs through the extracellular interaction between RP105–MD-1 and TLR4–MD-2 (ref. 20). Here, we propose two potential sTLR4–MD-2 binding sites on sRP105–MD-1 (**Fig. 7**). First, the binding site might be a composite surface of MD-1<sub>a</sub> and sRP105<sub>b</sub> (loops AB, CD, GH in MD-1<sub>a</sub> and the descending side of N-terminal domain in sRP105<sub>b</sub>), or vice versa, which is generated only after homodimerization (model 1; **Fig. 7a**). This model would explain why sRP105–MD-1 evolved a unique 2:2 organization rather than the 1:1 stoichiometry observed in sTLR4–MD-2. In this model, RP105–MD-1 mainly binds and occludes the

homodimerization interface of TLR4–MD-2–LPS, thereby preventing formation of a signaling-competent 2:2 complex through a direct competition mechanism. Alternatively, RP105–MD-1 may interfere with the accessibility of LPS to MD-2 by closing off the entrance to the MD-2 cavity (**Fig. 7a**)<sup>20</sup>. Model 1 is consistent with previous co-immunoprecipitation data that suggested direct MD-1–MD-2 interaction<sup>20</sup>. The second model is based on close evolutionary relatedness between RP105–MD-1 and TLR4–MD-2. This model proposes that the TLR4–MD-2 binding site is located in the sRP105 C-terminal domain and the MD-1 EF and GH loops that are equivalent to the homodimerization interface of sTLR4–MD-2–LPS<sup>10</sup> (model 2; **Figs. 6d** and **7b**). The RP105–MD-1 regions would make contacts with the counterparts of TLR4–MD-2 in a pseudosymmetric manner, engaging sRP105<sub>a</sub>–MD-1<sub>a</sub> (or sRP105<sub>b</sub>–MD-1<sub>b</sub>) and sTLR4–MD-2 with a similar molecular organization to the LPS-activated 2:2 TLR4–MD-2 complex. Similar to model 1, RP105–MD-1 may competitively inhibit LPS-induced TLR4–MD-2 oligomerization by occluding the homodimerization interface of TLR4–MD-2–LPS. Moreover, model 2 also explains how RP105–MD-1 inhibits LPS binding to TLR4–MD-2 (ref. 20). In LPS-bound 2:2 sTLR4–MD-2, one of LPS<sub>a</sub> acyl chains bulges out of the MD-2<sub>a</sub> cavity and is stabilized through hydrophobic interactions with apolar sTLR4<sub>b</sub> residues, including Phe440, Phe444 and Phe463 (**Supplementary Fig. 7**). However, these three apolar TLR4 residues are substituted with polar residues in RP105. Thus, the corresponding hydrophilic surface of RP105 could not stabilize the exposed hydrophobic LPS acyl chain, thereby disfavoring LPS binding to TLR4–MD-2. Because RP105–MD-1 forms a symmetric homodimer, one 2:2 RP105–MD-1 complex could provide two TLR4–MD-2 binding sites (**Fig. 7**). In both models, distances between the C termini of two sTLR4 chains are 140–150 Å, suggesting that two TLR4 molecules complexed with RP105–MD-1 are not competent to signal into cells and consistent with the inhibitory role of RP105–MD-1 in TLR4 signaling.

Furthermore, recent reports of MD-1 interaction with LPS<sup>33</sup> and an LPS-precursor lipid IVa<sup>32,33</sup>, combined with the structural conservation of the lipid recognition mode between MD-1 (ref. 33) and TLR4–MD-2 (ref. 10), allow us to propose that RP105–MD-1 can directly interact with LPS to sequester TLR4–MD-2 from LPS

signaling. In MD-1 complexed with tetra-acylated lipid IVa, one of its acyl chains is exposed out of the MD-1 cavity<sup>33</sup>, as in hexa-acylated LPS in sTLR4–MD-2 (ref. 10). Although the exact binding mode of LPS to RP105–MD-1 remains to be revealed, structures of MD-2 complexed with pseudoligands<sup>15</sup>, lipid IVa<sup>15</sup> and LPS<sup>10</sup> suggest that when LPS binds RP105–MD-1, LPS would have to rearrange the binding site to accommodate its six acyl chains, compared to pseudoligands or lipid IVa. In this scenario, LPS head groups would be displaced from the MD-1 cavity, and LPS acyl chains would protrude more out of the cavity. We expect that the exposed acyl chain would favor heterodimerization of RP105–MD-1 and TLR4–MD-2 (model 2 in Fig. 7b), as it mediates homodimerization of TLR4–MD-2 (ref. 10). Because model 2 explains the regulation of LPS response by RP105–MD-1 regardless of LPS binding, model 2 presently seems more plausible to us. Additionally, model 2 provides further insights into how RP105–MD-1 promotes the TLR2-mediated response to *M. tuberculosis* lipoprotein<sup>28</sup>. When TLR2 is substituted for TLR4 in model 2, its lipopeptide binding site is located close to the MD-1 cavity that has already been shown to accommodate diverse lipid molecules, raising the possibility that MD-1 would facilitate lipoprotein transfer to TLR2 to enhance the TLR2-mediated lipoprotein response<sup>6,8,32,33</sup>.

Our analysis implies that heterodimerization of RP105–MD-1 and TLR4–MD-2 and the subsequent reduction in LPS response would be favored only when LPS is bound to MD-1 but not to MD-2. Notwithstanding, dimerization of the C-terminal domains of TLR4 and RP105 would essentially block signaling in either scenario of LPS being bound to MD-2 or MD-1. Therefore, the question remains as to how LPS triggers formation of the inhibitory complex. Is it by RP105–MD-1–LPS having higher affinity for TLR4–MD-2, or by TLR4–MD-2–LPS having higher affinity for RP105–MD-1? Furthermore, the strict symmetry of the dimeric interaction, as in TLR4–MD-2–LPS, would not be maintained in the RP105–TLR4 heterodimer. Thus, many fascinating questions are now raised by these unexpected findings, and future structural and mutational studies on the interaction between RP105–MD-1 and TLR4–MD-2, in the presence and absence of LPS, are required to determine the exact regulatory mechanism of RP105 and the precise biological role of the 2:2 RP105–MD-1 complex.

## METHODS

Methods and any associated references are available in the online version of the paper at <http://www.nature.com/nsmb/>.

**Accession codes.** Protein Data Bank: coordinates and structure factors have been deposited for bovine sRP105–MD-1 with the accession code 3RG1.

*Note: Supplementary information is available on the Nature Structural & Molecular Biology website.*

## ACKNOWLEDGMENTS

We thank R.L. Stanfield (The Scripps Research Institute) and Y.S. Choo (Sanford-Burnham Medical Research Institute) for critical comments on the manuscript, R.L. Stanfield (The Scripps Research Institute), H. Tien and D. Marciano (The Joint Center for Structural Genomics) for automated crystal screening, and X. Dai and M.A. Elsliger (The Scripps Research Institute) for expert technical assistance. The work was supported by US National Institutes of Health grant AI042266 (to I.A.W.) and the Skaggs Institute for Chemical Biology. X-ray diffraction datasets were collected at the Stanford Synchrotron Radiation Lightsource beamline 9-2 and the Advanced Photon Source beamline 23ID-B. This is manuscript no. 20749 from The Scripps Research Institute.

## AUTHOR CONTRIBUTIONS

S.Y. and I.A.W. designed experiments. S.Y. and M.H. conducted experiments. S.Y., M.H. and I.A.W. analyzed data and wrote the manuscript.

## COMPETING FINANCIAL INTERESTS

The authors declare no competing financial interests.

Published online at <http://www.nature.com/nsmb/>.

Reprints and permissions information is available online at <http://www.nature.com/reprints/index.html>.

- Bell, J.K. *et al.* Leucine-rich repeats and pathogen recognition in Toll-like receptors. *Trends Immunol.* **24**, 528–533 (2003).
- Takeda, K., Kaisho, T. & Akira, S. Toll-like receptors. *Annu. Rev. Immunol.* **21**, 335–376 (2003).
- Proell, M., Riedl, S.J., Fritz, J.H., Rojas, A.M. & Schwarzenbacher, R. The Nod-like receptor (NLR) family: a tale of similarities and differences. *PLoS ONE* **3**, e2119 (2008).
- Nakhaei, P., Genin, P., Civas, A. & Hiscott, J. RIG-I-like receptors: sensing and responding to RNA virus infection. *Semin. Immunol.* **21**, 215–222 (2009).
- Kim, H.M. *et al.* Crystal structure of the TLR4–MD-2 complex with bound endotoxin antagonist Eritoran. *Cell* **130**, 906–917 (2007).
- Jin, M.S. *et al.* Crystal structure of the TLR1–TLR2 heterodimer induced by binding of a tri-acylated lipopeptide. *Cell* **130**, 1071–1082 (2007).
- Choe, J., Kelker, M.S. & Wilson, I.A. Crystal structure of human toll-like receptor 3 (TLR3) ectodomain. *Science* **309**, 581–585 (2005).
- Kang, J.Y. *et al.* Recognition of lipopeptide patterns by Toll-like receptor 2–Toll-like receptor 6 heterodimer. *Immunity* **31**, 873–884 (2009).
- Bell, J.K. *et al.* The molecular structure of the Toll-like receptor 3 ligand-binding domain. *Proc. Natl. Acad. Sci. USA* **102**, 10976–10980 (2005).
- Park, B.S. *et al.* The structural basis of lipopolysaccharide recognition by the TLR4–MD-2 complex. *Nature* **458**, 1191–1195 (2009).
- Liu, L. *et al.* Structural basis of toll-like receptor 3 signaling with double-stranded RNA. *Science* **320**, 379–381 (2008).
- Shimazu, R. *et al.* MD-2, a molecule that confers lipopolysaccharide responsiveness on Toll-like receptor 4. *J. Exp. Med.* **189**, 1777–1782 (1999).
- Nagai, Y. *et al.* Essential role of MD-2 in LPS responsiveness and TLR4 distribution. *Nat. Immunol.* **3**, 667–672 (2002).
- Poltorak, A. *et al.* Defective LPS signaling in C3H/HeJ and C57BL/10ScCr mice: mutations in *Tlr4* gene. *Science* **282**, 2085–2088 (1998).
- Ohto, U., Fukase, K., Miyake, K. & Satow, Y. Crystal structures of human MD-2 and its complex with antiendotoxin lipid IVa. *Science* **316**, 1632–1634 (2007).
- Mullarkey, M. *et al.* Inhibition of endotoxin response by e5564, a novel Toll-like receptor 4-directed endotoxin antagonist. *J. Pharmacol. Exp. Ther.* **304**, 1093–1102 (2003).
- Miyake, K., Yamashita, Y., Ogata, M., Sudo, T. & Kimoto, M. RP105, a novel B cell surface molecule implicated in B cell activation, is a member of the leucine-rich repeat protein family. *J. Immunol.* **154**, 3333–3340 (1995).
- Miura, Y. *et al.* Molecular cloning of a human RP105 homologue and chromosomal localization of the mouse and human RP105 genes (Ly64 and LY64). *Genomics* **38**, 299–304 (1996).
- Fugier-Vivier, I. *et al.* Molecular cloning of human RP105. *Eur. J. Immunol.* **27**, 1824–1827 (1997).
- Divanovic, S. *et al.* Negative regulation of Toll-like receptor 4 signaling by the Toll-like receptor homolog RP105. *Nat. Immunol.* **6**, 571–578 (2005).
- Miura, Y. *et al.* RP105 is associated with MD-1 and transmits an activation signal in human B cells. *Blood* **92**, 2815–2822 (1998).
- Miyake, K. *et al.* Mouse MD-1, a molecule that is physically associated with RP105 and positively regulates its expression. *J. Immunol.* **161**, 1348–1353 (1998).
- Nagai, Y. *et al.* Requirement for MD-1 in cell surface expression of RP105/CD180 and B-cell responsiveness to lipopolysaccharide. *Blood* **99**, 1699–1705 (2002).
- Nagai, Y. *et al.* The radioprotective 105/MD-1 complex links TLR2 and TLR4/MD-2 in antibody response to microbial membranes. *J. Immunol.* **174**, 7043–7049 (2005).
- Ogata, H. *et al.* The toll-like receptor protein RP105 regulates lipopolysaccharide signaling in B cells. *J. Exp. Med.* **192**, 23–29 (2000).
- Divanovic, S. *et al.* Regulation of TLR4 signaling and the host interface with pathogens and danger: the role of RP105. *J. Leukoc. Biol.* **82**, 265–271 (2007).
- Divanovic, S. *et al.* Inhibition of TLR-4/MD-2 signaling by RP105/MD-1. *J. Endotoxin Res.* **11**, 363–368 (2005).
- Blumenthal, A. *et al.* RP105 facilitates macrophage activation by *Mycobacterium tuberculosis* lipoproteins. *Cell Host Microbe* **5**, 35–46 (2009).
- Hindle, K.L., Bella, J. & Lovell, S.C. Quantitative analysis and prediction of curvature in leucine-rich repeat proteins. *Proteins* **77**, 342–358 (2009).
- Bublitz, M. *et al.* Crystal structure and standardized geometric analysis of InIJ, a listerial virulence factor and leucine-rich repeat protein with a novel cysteine ladder. *J. Mol. Biol.* **378**, 87–96 (2008).
- Enkhbayar, P., Kamiya, M., Osaki, M., Matsumoto, T. & Matsushima, N. Structural principles of leucine-rich repeat (LRR) proteins. *Proteins* **54**, 394–403 (2004).
- Harada, H., Ohto, U. & Satow, Y. Crystal structure of mouse MD-1 with endogenous phospholipid bound in its cavity. *J. Mol. Biol.* **400**, 838–846 (2010).
- Yoon, S.I., Hong, M., Han, G.W. & Wilson, I.A. Crystal structure of soluble MD-1 and its interaction with lipid IVa. *Proc. Natl. Acad. Sci. USA* **107**, 10990–10995 (2010).
- Altmann, F., Staudacher, E., Wilson, I.B. & Marz, L. Insect cells as hosts for the expression of recombinant glycoproteins. *Glycoconj. J.* **16**, 109–123 (1999).
- Aeed, P.A. & Elhammer, A.P. Glycosylation of recombinant prorenin in insect cells: the insect cell line Sf9 does not express the mannose 6-phosphate recognition signal. *Biochemistry* **33**, 8793–8797 (1994).
- Lawrence, M.C. & Colman, P.M. Shape complementarity at protein/protein interfaces. *J. Mol. Biol.* **234**, 946–950 (1993).



## ONLINE METHODS

**Expression and purification of sRP105–MD-1.** Bovine, human and mouse sRP105–MD-1 complexes were expressed extracellularly by a baculovirus expression system using a modified dual expression vector, pAcUW51 (BD Biosciences). The expression vector encodes MD-1 attached to the C-terminal thrombin cleavage site and the Strep-tag II, and sRP105 attached to the C-terminal thrombin cleavage site and the His<sub>6</sub>-tag. To generate sRP105–MD-1-expressing baculovirus, Sf9 insect cells were co-transfected with the expression vector DNA and the linearized baculovirus DNA, ProFold-ER1 (AB vector). The sRP105 and MD-1 proteins were expressed for 2 d after infecting Sf9 or High Five cells with amplified recombinant virus. Secreted protein was purified by Ni-NTA (Qiagen) affinity chromatography and Strep-Tactin (IBA) affinity chromatography. After C-terminal tag cleavage by thrombin, the resulting protein was further purified by gel filtration chromatography. The purified proteins were screened for crystallization, but only bovine sRP105–MD-1 generated diffraction quality crystals. As an alternative expression to verify the sRP105–MD-1 homodimerization interaction, mouse sRP105 and mouse MD-1 (or its mutants, G52D or G71D) were simultaneously expressed by coinfection of High Five insect cells with sRP105- and MD-1-expressing baculoviruses. The individual baculoviruses were generated using a modified pAcGP67 transfer vector that contains the C-terminal thrombin cleavage site and the His<sub>6</sub>-tag. The expressed sRP105 and MD-1 proteins were initially purified by Ni-NTA affinity chromatography and the resulting proteins were analyzed by gel filtration chromatography using a Superdex 200 HR 10/30 gel filtration column.

To improve the X-ray diffraction quality of bovine sRP105–MD-1 crystals beyond ~4 Å, reductive methylation of lysine residues was applied to the Strep-Tactin column-purified bovine sRP105–MD-1 complex (residues 24–626 and 22–159, respectively), as previously described<sup>37</sup>. The resultant dimethylated protein complex was further purified by gel filtration chromatography. The methylated complex protein was used to derive the final sRP105–MD-1 structure to 2.91 Å resolution.

Analytical gel filtration analysis showed that lysine methylation did not alter the oligomeric status of the sRP105–MD-1 complex. Furthermore, the effect of lysine methylation on the sRP105–MD-1 binding interfaces would be minimal, because methyl groups are small and a lysine residue is able to make a hydrogen bond even after methylation ( $pK_a$  of unmethylated lysine, 10.2;  $pK_a$  of dimethyl lysine, 10.2–10.4)<sup>38</sup>. However, there is a possibility that methylation may alter the hydrogen bond status of two interface residues (Lys353 in primary interface B and Lys113 in primary interface A) from bi- or trifurcated hydrogen bonds to single hydrogen bonds.

To obtain a different crystal lattice that could provide initial, additional phase information, 11 sRP105-VLR hybrids were designed by fusing the N-terminal region of bovine sRP105 to the C-terminal region of hagfish VLR B.61, in a design previously reported for other TLRs<sup>5,6,8,39</sup>. They were co-expressed and co-purified with bovine MD-1 (residues 22–159), as for the wild-type complex. One of sRP105-VLR hybrids (sRP105 residues 24–521 and VLR B.61 residues 125–200) provided a sufficient amount of protein for structural studies, and its complex with MD-1 was used to obtain experimental phases.

**Crystallization and data collection.** sRP105-VLR–MD-1 and methylated sRP105–MD-1 were crystallized at 23 °C by sitting drop vapor diffusion in

space groups  $P2_12_12_1$  and  $P1$  with one and four 2:2 complexes, respectively, in the asymmetric unit. The sRP105-VLR–MD-1 crystals were obtained by mixing 0.5 µl of 10 mg ml<sup>-1</sup> protein solution with 0.5 µl of well solution containing 20% w/v PEG MME 5000, 0.2 M NH<sub>4</sub>Cl and 100 mM sodium acetate, pH 4.6. Heavy atom derivative crystals were prepared for experimental phasing by soaking sRP105-VLR–MD-1 crystals in 1 mM K<sub>2</sub>Pt(NO<sub>2</sub>)<sub>4</sub> solution. X-ray diffraction data on the platinum derivative were collected at peak wavelength (1.0718 Å) at 100 K at the Stanford Synchrotron Radiation Lightsource (SSRL) beamline 9-2. The methylated sRP105–MD-1 complex was crystallized in a drop containing 1 µl of 10–mg ml<sup>-1</sup> protein solution and 1 µl of well solution containing 19% (w/v) PEG 8000 and 100 mM Tris, pH 8.5. The sRP105–MD-1 diffraction data were collected at a wavelength of 1.0333 Å at 100 K at the Advanced Photon Source (APS) beamline 23ID-B. X-ray data were processed with HKL2000 (ref. 40). Data collection statistics are summarized in **Table 1**.

**Structure determination and refinement.** The sRP105-VLR–MD-1 structure was determined by a single-wavelength anomalous diffraction (SAD) phasing experiment conducted on a platinum derivative crystal. Eleven heavy atom sites were located by SHELXD<sup>41</sup> and phases were calculated by SHELXE<sup>41</sup>. The initial model of the 2:2 sRP105-VLR–MD-1 complex was built by docking and modifying the structures of chicken MD-1 (PDB 3MTX)<sup>33</sup> and mouse sTLR4 (PDB 2Z64)<sup>5</sup> against the electron density map obtained from dm<sup>42</sup>. The sRP105-VLR–MD-1 model was built with Coot<sup>43</sup> and refined with REFMAC5 (ref. 44). The sRP105–MD-1 structure was determined by molecular replacement with PHASER<sup>45</sup> using the 1:1 sRP105-VLR–MD-1 structure as a search model. Iterative model building and refinement were conducted using Coot<sup>43</sup> and REFMAC5 (ref. 44), respectively. The Ramachandran plot generated with MolProbity (<http://molprobity.biochem.duke.edu/>) shows that 93.9% of residues are in favored regions with only 0.3% as outliers. Final refinement statistics are summarized in **Table 1**. All the molecular graphic figures were made using PyMOL (<http://www.pymol.org/>).

37. Walter, T.S. *et al.* Lysine methylation as a routine rescue strategy for protein crystallization. *Structure* **14**, 1617–1622 (2006).
38. Jentoft, N. & Dearborn, D.G. Protein labeling by reductive alkylation. *Methods Enzymol.* **91**, 570–579 (1983).
39. Jin, M.S. & Lee, J.O. Application of hybrid LRR technique to protein crystallization. *BMB Rep* **41**, 353–357 (2008).
40. Otwinowski, Z. & Minor, W. Processing of X-ray diffraction data collected in oscillation mode. *Methods Enzymol.* **276**, 307–326 (1997).
41. Sheldrick, G.M. A short history of SHELX. *Acta Crystallogr. A* **64**, 112–122 (2008).
42. Cowtan, K. 'dm': an automated procedure for phase improvement by density modification. *Joint CCP4 and ESF-EACBM Newslett. on Protein Crystallogr.* **31**, 34–38 (1994).
43. Emsley, P. & Cowtan, K. Coot: model-building tools for molecular graphics. *Acta Crystallogr. D Biol. Crystallogr.* **60**, 2126–2132 (2004).
44. Murshudov, G.N., Vagin, A.A. & Dodson, E.J. Refinement of macromolecular structures by the maximum-likelihood method. *Acta Crystallogr. D Biol. Crystallogr.* **53**, 240–255 (1997).
45. McCoy, A.J. *et al.* Phaser crystallographic software. *J. Appl. Crystallogr.* **40**, 658–674 (2007).